Dalton Transactions

PAPER

View Article Online
View Journal | View Issue

Cite this: *Dalton Trans.*, 2014, **43**, 17677

Electron transfer dynamics and excited state branching in a charge-transfer platinum(II) donor–bridge-acceptor assembly†

Paul A. Scattergood,‡[a] Milan Delor,‡[a] Igor V. Sazanovich,[a,b] Oleg V. Bouganov,[c] Sergei A. Tikhomirov,[c] Alexander S. Stasheuski,[c] Anthony W. Parker,[b] Gregory M. Greetham,[b] Michael Towrie,[b] E. Stephen Davies,[d] Anthony J. H. M. Meijer*[a] and Julia A. Weinstein*[a]

A linear asymmetric Pt(II) *trans*-acetylide donor–bridge-acceptor triad designed for efficient charge separation, NAP≡Pt(PBu$_3$)$_2$≡Ph–CH$_2$–PTZ (**1**), containing strong electron acceptor and donor groups, 4-ethynyl-*N*-octyl-1,8-naphthalimide (NAP) and phenothiazine (PTZ) respectively, has been synthesised and its photoinduced charge transfer processes characterised in detail. Excitation with 400 nm, ~50 fs laser pulse initially populates a charge transfer manifold stemming from electron transfer from the Pt-acetylide centre to the NAP acceptor and triggers a cascade of charge and energy transfer events. A combination of ultrafast time-resolved infrared (TRIR) and transient absorption (TA) spectroscopies, supported by UV-Vis/IR spectroelectrochemistry, emission spectroscopy and DFT calculations reveals a self-consistent photophysical picture of the excited state evolution from femto- to milliseconds. The characteristic features of the NAP-anion and PTZ-cation are clearly observed in both the TRIR and TA spectra, confirming the occurrence of electron transfer and allowing the rate constants of individual ET-steps to be obtained. Intriguingly, **1** has three separate ultrafast electron transfer pathways from a non-thermalised charge transfer manifold directly observed by TRIR on timescales ranging from 0.2 to 14 ps: charge recombination to form either the intraligand triplet ^{3}NAP with 57% yield, or the ground state, and forward electron transfer to form the full charge-separated state ^{3}CSS (^{3}[PTZ$^+$–NAP$^-$]) with 10% yield as determined by target analysis. The ^{3}CSS decays by charge-recombination to the ground state with ~1 ns lifetime. The lowest excited state is ^{3}NAP, which possesses a long lifetime of 190 μs and efficiently sensitises singlet oxygen. Overall, molecular donor–bridge-acceptor triad **1** demonstrates excited state branching over 3 different pathways, including formation of a long-distant (18 Å) full charge-separated excited state from a directly observed vibrationally hot precursor state.

Received 6th June 2014,
Accepted 20th October 2014

DOI: 10.1039/c4dt01682c

www.rsc.org/dalton

Introduction

Photoinduced electron transfer, an elementary process, underpins a variety of applications, especially in light-harvesting, photocatalysis, and optoelectronics. The process of electron transfer can be extremely fast, occurring on sub-picosecond timescales and as such has been widely studied by ultrafast spectroscopic methods to follow excited state dynamics in real time.[1] The mechanism of intramolecular photoinduced electron transfer usually involves the formation of a charge-separated excited state (CSS).[2,3] A CSS is formed upon a shift of electron density from an electron donor D to an electron acceptor A, often *via* a connecting "bridging" unit which can play a major role in mediating charge transfer.

[a]*Department of Chemistry, University of Sheffield, Sheffield, S3 7HF, UK. E-mail: Julia.Weinstein@sheffield.ac.uk, A.Meijer@sheffield.ac.uk*
[b]*Central Laser Facility, Research Complex at Harwell, Rutherford Appleton Laboratory, Research Complex at Harwell, Harwell Science and Innovation Campus, Chilton, Oxfordshire OX11 0QX, UK*
[c]*B.I. Stepanov Institute of Physics, 68 Nezavisimosti Ave., Minsk, 220072, Belarus*
[d]*School of Chemistry, The University of Nottingham, Nottingham NG7 2RD, UK*

†Electronic supplementary information (ESI) available: Detail on synthesis, NMR, electrochemistry, CV for all compounds. Emission data for **1** and **3** in toluene. IR spectroelectrochemistry for **3**. Further ultrafast spectroscopy analysis, including decay associated spectra resulting from global analysis. Full computational details including IR spectra for the non-truncated structure of **2**, all structures, coordinates, electronic transitions and molecular orbitals. Details of ultrafast TRIR and transient absorption setups. See DOI: 10.1039/c4dt01682c

‡These authors contributed equally to the work presented herein.

Extensive assemblies designed on this principle, which contain multiple donor and acceptor units of gradually increased D/A strength, act as model systems for investigating charge transfer events, similar to those observed in photosynthesis. Transition metal donor–bridge-acceptor (DBA) molecular triads and their multi-donor/acceptor relatives have proven to be an effective design motif in which a photoinduced CSS can be attained.[2,4–10]

There is currently much interest in understanding the behaviour and energy relaxation processes that occur immediately after light absorption. Electron transfer from a non-thermalised manifold, which competes with vibrational relaxation in the excited state, is one such process.[11] Time-resolved broadband infrared spectroscopy (TRIR), a method where an excited state is optically prepared by a UV/Vis pulse and probed by a broadband IR pulse, is particularly suited to investigate such dynamics. Recent developments in ultrafast TRIR permit broad spectral coverage and simultaneous observation of the dynamics of several infrared reporting groups, expanding significantly the range of excited state processes which can be followed directly.[12–15] This paper demonstrates how selective strong IR chromophores within Pt(II) based molecular assemblies permit characterisation of ultrafast electron transfer, and direct observation of an effect of excited state branching from vibrationally hot electronic states.

The use of Pt(II) containing bridging units is particularly attractive for ultrafast ET investigations owing to the square planar coordination environment around the metal centre which provides synthetic versatility for the specific attachment of ligands, and enables control over the directionality of electron transfer.[14–16] The utilisation of donor acetylide ligands in particular facilitates the formation of more stable, longer-lived charge-separated states due to strong-field acetylides raising the energy of a deactivating dd-state, and led to a large family of *cis* bis-acetylide Pt(II) complexes employing redox-active diimine acceptor ligands.[16–21]

Here we investigate light-induced processes in a linear, asymmetric *trans* acetylide donor–acceptor Pt(II) triad **1**, Fig. 1.[22] Our design employs a neutral co-ligand phosphine,[23–32] which lacks low lying π^* orbitals hence does not engage in the charge-transfer processes between the *trans* configured donor and acceptor ligands, ensuring that the light-harvesting system has a pre-conditioned charge transfer directionality. A number of Pt(II) bis-phosphine complexes with a *trans* arrangement of the two identical acetylides[9,33–44] has been reported, largely driven by their applications in optoelectronics and optical power limiting. Examples of *asymmetric* [donor-C≡C–Pt–C≡C-acceptor] motifs include complexes incorporating a triarylamine electron donor and an oxadiazole based electron acceptor,[23] ethynyl-naphthalimide electron acceptor and phenyl-acetylene

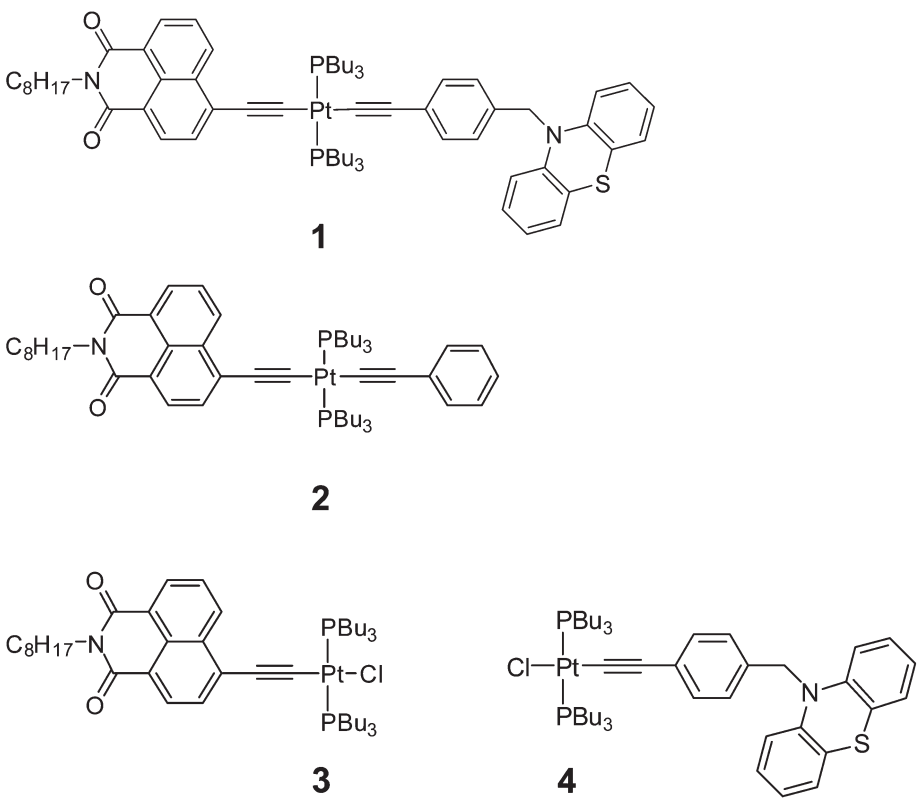

Fig. 1 The Pt(II) acetylide complexes investigated in this study: the donor–bridge-acceptor triad NAP≡Pt(PBu$_3$)$_2$≡Ph–CH$_2$–PTZ ('NAP–Pt–PTZ', **1**), and its analogs and precursors NAP≡Pt(PBu$_3$)$_2$≡Ph ('NAP–Pt–Ph', **2**), NAP≡Pt(PBu$_3$)$_2$–Cl ('NAP–Pt–Cl', **3**), and Cl–Pt(PBu$_3$)$_2$≡Ph–CH$_2$–PTZ ('Cl–Pt–PTZ', **4**).

co-ligand,[31] a (diphenylamino)-2,7-fluorenylene (DPAF) electron donor and a naphthalene diimide (NDI) electron acceptor,[45] and some more elaborate assemblies.[34,46,47]

The triad **1** combines a strong electron acceptor 4-ethynyl-*N*-octyl-1,8-naphthalimide (NAP) and an electron donor phenothiazine (PTZ). Aromatic acid imide acceptor groups have been used in diverse charge-transfer assemblies[21,48–50] owing to their low reduction potentials, and the ability to form stable radical-anions which possess distinct and intense absorptions in both UV-Vis and IR spectral ranges.[48,51,52] Likewise, the donor PTZ is readily oxidised, forming a stable radical cation which has a distinct absorption in the visible range.[53–56] To enable a step-wise charge-transfer process, the donor moiety in **1** is connected to the Pt-acetylide bridge through a saturated linker. The elucidation of light-induced processes in **1** was assisted by a detailed study of the "building blocks" **2–4**, which contain only the acceptor fragment (**3**), the acceptor and the bis-acetylide Ph–C≡C–Pt–C≡C-bridge (**2**), and only the donor fragment (**4**), Fig. 1.

The presence of strong IR reporters – the ν(C=O) of the imide electron acceptor as well as ν(C≡C) positioned on both D and A molecular fragments – enable the use of ultrafast TRIR for monitoring excited state dynamics and intermediate states. The combination of vibrational spectroscopy with time-resolved electronic transient absorption spectroscopy (TA) along with UV/Vis/IR (spectro)electrochemical and computational methods resolves the rich photophysics of the charge-transfer assemblies, involving multiple excited states evolving across the femto-to-millisecond time range.

Results and discussion

Synthesis

1 and **2** were prepared through a stepwise approach *via* the "acceptor-bridge" dyad **3**. In turn, **3** and the "donor-bridge" dyad **4** were prepared from *cis*-Pt$(PBu_3)_2Cl_2$. All four complexes contain a common *trans*-Pt(II) bis phosphine core. The Pt-containing starting material *cis*-Pt$(PBu_3)_2Cl_2$ was prepared *via* the reaction of $PtCl_2$ with a slightly sub-stoichiometric quantity of P^nBu_3 at r.t. to yield the four-coordinate complex in moderate yields (60–70%) with absolute *cis* stereochemistry. This route allows one to perform the reaction on a smaller scale in comparison to the procedure employing K_2PtCl_4 where the use of small quantities of reagents was reported to decrease the product yield.[57]

It should be noted that the commonly used copper-assisted Hagihara type coupling results in predominantly bis substitution at the Pt centre to give symmetrical *trans* acetylide products in a statistical mixture. Therefore, amine mediated high temperature reaction conditions were employed instead to produce asymmetric mono-substituted Pt(II) acetylides[24,31,58] which then can be functionalised with another acetylide ligand. Thus, [*trans*-acetylide-Pt–Cl] dyads **3** and **4** were formed in a reaction of *cis*-Pt$(PBu_3)_2Cl_2$ with 4-ethynyl-*N*-octyl-1,8-naphthalimide[59] and *N*-(4-ethynylbenzyl)-phenothiazine,[60] respectively, in boiling $^iPr_2NH$ in the absence of CuI.

1 and **2** were formed directly from **3** utilising the CuI assisted cross coupling procedure[61,62] to coordinate either phenylacetylene or an ethynyl moiety containing *N*-(4-ethynylbenzyl)-phenothiazine. Both syntheses proceeded with moderate to high yields, affording bright yellow coloured products which were purified *via* column chromatography and satisfactorily characterised through NMR and mass spectrometry. ^{31}P NMR yields J_{Pt-P} values in the region of 2300 Hz that are indicative of the *trans* geometry of the phosphine groups at the metal centre. Conversely, significantly larger coupling ($J_{Pt-P} \approx$ 3500 Hz) is noted for *cis* phosphine configurations such as that present in the $Pt(PBu_3)_2Cl_2$ precursor material.[63] We highlight that despite starting from a *cis* phosphine precursor complex, **1–3** were found to be formed with *trans* stereochemistry. No *cis* isomers were isolated nor has any isomerisation been observed either in solution or after exposure to visible light.

Electrochemistry

In order to determine the nature and the energy of the frontier orbitals, cyclic voltammetry studies were performed for solutions of **1–4** in CH_2Cl_2 across the potential window from −2.2 to +1.3 V (Fig. S1a,† Table 1).

Complexes **1–3** show one electrochemically quasi-reversible process at −1.83 V assigned to reduction of the naphthalimide group,[53] an assignment supported by the results of DFT calculations (*vide infra*). The potential of this reduction is unaffected by the group positioned mutually *trans* to the NAP functionality indicating a lack of electronic communication through the metal-acetylide centre in the electronic ground state. Compound **4** displays no reduction processes within the potential range studied.

Complexes **1** and **4** each display an electrochemically reversible process at *ca.* +0.35 V assigned as an oxidation based on the phenothiazine (PTZ) functionality.[54,55,60,64,65] This value is consistent with a potential of +0.37 V found for the PTZ containing ethynyl ligand ('PTZ-H') and the iodide terminated synthetic precursor ('PTZ-I') (see ESI†).

Table 1 Electrochemical data (*vs.* Fc^+/Fc) for 1.65 mM CH_2Cl_2 solutions of complexes **1–4** containing 0.2 M $[NBu_4][PF_6]$ as supporting electrolyte. Anodic/cathodic peak separations for reversible processes are shown in brackets

Complex	Reduction [V]	Oxidation [V]
1	−1.83 (0.14)	+0.34 (0.09)[b], +0.94[a], +1.13[a]
2	−1.83 (0.13)	+0.87[a]
3	−1.83 (0.13)	+1.14[a]
4[c]	—	+0.35 (0.08), +1.07[a]

[a] Irreversible oxidation process, the anodic peak potential is quoted. [b] Process found to be reversible when isolated across the potential range −0.5 to + 0.7 V. [c] In CH_2Cl_2 containing 0.4 M $[NBu_4][BF_4]$; anodic/cathodic peak separation for the Fc^+/Fc couple used as the internal standard was 0.08 V.

A single, irreversible oxidation observed for **2** and **3** at +0.87 and +1.14 V, respectively, is assigned in both complexes to oxidation of a central Pt-acetylide unit, an electrochemical feature which has been readily observed in a number of previously reported Pt(II) acetylide complexes.[19,54,60,66–68] The PTZ-containing compounds **1** and **4** also have additional oxidation processes in the range from +0.94 V to +1.13 V (Table 1), which could not be assigned with confidence due to their electrochemically irreversible nature. From the CV data, the HOMO and LUMO for **1** are based on the PTZ and NAP groups, respectively, allowing an estimate of 2.17 V for the energy of the lowest charge-separated excited state [PTZ^{+}–NAP^{-}].

UV/Vis absorption spectroscopy

The ground-state absorption spectra of complexes **1–4** in CH_2Cl_2 (Fig. 2) in the region from 240 to 350 nm are dominated by high energy intraligand π–π* transitions. Comparison of the spectra of the individual molecular units shows that the transition centered at 320 nm is present in the spectra of **1**, **2** and **4** but not of **3** and therefore we assign this spectral component to phenyl and PTZ π–π* transitions, also observed in the starting PTZ-H ligand. The lowest energy transition in **3**, observed at 424 nm, is assigned to a metal-to-ligand charge transfer (MLCT) transition from the Pt/acetylide center to the NAP moiety.[31,49] The relative broadness of this band suggests that there are several charge-transfer transitions contributing to the absorption envelope. In **1** and **2**, this band is broader and slightly red-shifted, to 430 nm. The absorption spectra for **1** and **2** in the visible region are virtually identical, suggesting that the lowest excited state corresponds to a mixed-metal-ligand-to-ligand charge transfer (ML/L′CT) manifold which involves the phenylacetylide fragment and the Pt center, but does not involve the PTZ fragment in **1**. These band assignments are confirmed by DFT calculations (*vide infra*), which show that in **1** and **2**, there are at least three transitions within the ~430 nm absorption envelope, all predominantly due to electron density shift from the central bridge C≡C–Pt–C≡C–Ph to the NAP moiety. The extinction coefficients at the maximum of the charge transfer bands are the same for **1–3** within instrumental error, $(42 \pm 1) \times 10^3$ dm^3 mol^{-1} cm^{-1}.

As the absorption spectrum of the Cl–Pt–PTZ model complex **4** does not have any bands at wavelengths longer than 350 nm, it follows that electronic excitation of **1** with >370 nm will exclusively populate a bridge-to-NAP charge transfer excited state manifold without initially affecting the PTZ part of the complex. Since this paper focuses on investigating the light-induced properties of DBA system **1** using wavelengths >400 nm, **4** which does not absorb at these wavelengths was not investigated further.

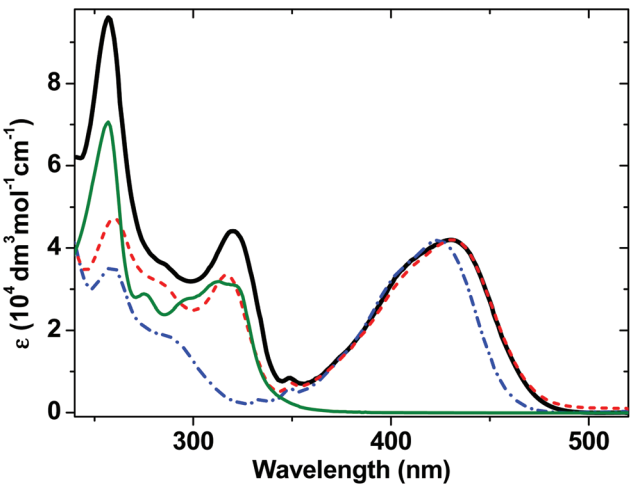

Fig. 2 UV/Vis absorption spectra for **1** (solid black line), **2** (red dashed line) and **3** (blue dot-dashed line), and **4** (thin dark green line) in CH_2Cl_2 at r.t.

Emission spectroscopy (Table 2)

Complexes **1–3** display dual emission. A high energy structureless emission band is centered at 518 nm for **1**, 522 nm for **2** and 498 nm for **3**. A lower energy emission band has a clearly defined vibronic structure, with a first component at ~640 nm in CH_2Cl_2 at r.t. (Fig. 3). These dual emission observations are consistent with those reported for the very close analogues of **2** and **3**,[31] and other *trans*-Pt(bis)acetylides.[41,69–71] The structured spectral profile of the low-energy emission band closely corresponds to the phosphorescence from the intraligand triplet localized on the NAP moiety (^{3}NAP).[31,49,72] This low-energy emission process is efficiently quenched by oxygen and is absent in aerated solution (Fig. S2†), which, along with its lack of solvatochromism, 190 microsecond lifetime, and the data from flash photolysis (Fig. S3†) and TRIR (see below), confirms its assignment to a ^{3}NAP state. The high-energy emission band maximum shifts from 518 to 481 nm (**1**) and from 498 to 461 nm (**3**) when the solvent is changed from CH_2Cl_2 to the less polar toluene (Fig. S2†), suggesting that this emission emanates from a charge-transfer state.

Emission lifetimes of the high energy emission band (estimated using the Edinburgh Instrument mini-τ, instrument

Table 2 Absorption and emission maxima, excited state lifetimes, and quantum yields of emission and singlet oxygen production for complexes **1–3**

Complex	λ_{abs} [nm]	λ_{em} [nm]	τ^a [ps]	τ^b [μs]	$\phi_{em}{}^c$ (%)	$^1O_2{}^d$ (%)
1	430	518	14 ± 1		0.1	
		640 (696, 775)^e		190 ± 10	5.5	57 ± 7
2	430	522	20 ± 1		0.2	
		640 (696, 775)^e		190 ± 10	7.4	82^f
3	424	498	209 ± 9		2.6	
		635 (693, 775)^e		190 ± 10	4.9	90 ± 10^g

^{a} Values averaged from the results of ultrafast transient absorption and TRIR. ^{b} From emission lifetime measurements under 424 nm excitation for **3** and 430 nm excitation for **1** and **2**. ^{c} Relative to a solution of $[Ru(bpy)_3]Cl_2$ in H_2O, ϕ_{em} = 0.028.[73] ^{d} Singlet oxygen quantum yields measured against reference compound perinaphthenone in CH_2Cl_2. ^{e} Vibronic progression indicated in brackets. ^{f} From ref. 31. ^{g} Same value as in ref. 31.

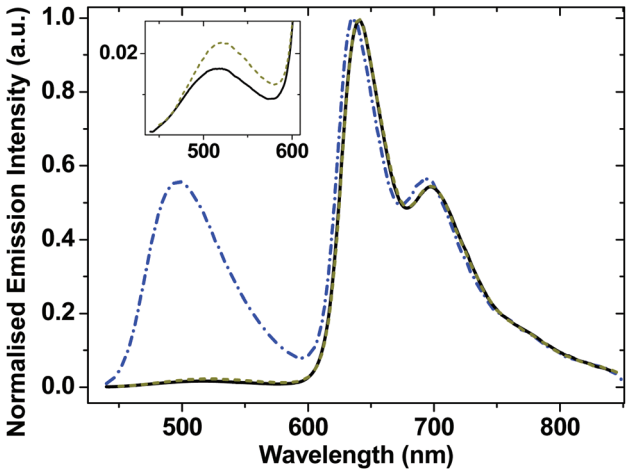

Fig. 3 Normalised emission spectra for degassed solutions of **1** (solid black line), **2** (dark yellow dashed line), and **3** (blue dot-dashed line) in CH_2Cl_2 and at r.t. The inset shows an expansion of the high-energy profiles for complexes **1** and **2**.

response function ≈80 ps) is ≈200 ± 50 ps for **3**, and instrument-limited for **1** and **2**. The short lifetime of the first emissive state is attributed to an ultrafast conversion into low-lying states which will be described in later sections. The lifetime of the emissive state responsible for the low-energy emission band is 190 μs (Fig. S3†).

Compounds **1–3** efficiently sensitise singlet oxygen under visible light, confirming the triplet nature of the lowest excited sate as ^{3}NAP. Singlet oxygen quantum yields (90% for **3**, 57% for **1**, Table 2) provide lower limit for the yield of the ^{3}NAP product state.

Fourier transform IR (FTIR) and IR spectroelectrochemistry

Ground state FTIR spectra of **1**, **2** and **3** in CH_2Cl_2 in the spectral range from 1475 to 2200 cm^{-1} (Fig. 4) are dominated by

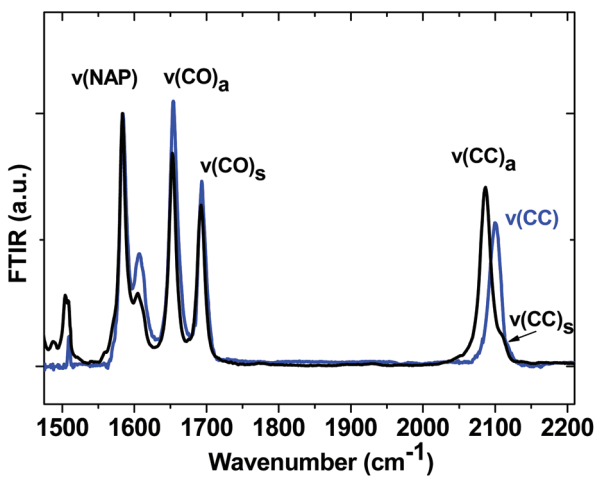

Fig. 4 Normalised Fourier-Transform IR (FTIR) spectra for **1** (black) and **3** (blue) in CH_2Cl_2 in the 1475 cm^{-1} to 2200 cm^{-1} region. The spectrum of **2** follows that of **1** very closely and is omitted for clarity.

NAP ring breathing modes ν(NAP) at 1583 cm^{-1} and asymmetric/symmetric combinations of the NAP-localised carbonyl vibrations ν(C═O) at 1652/1691 cm^{-1} in the fingerprint region. The presence of two acetylide moieties in **1** gives rise to asymmetric/symmetric combinations of the bridge-localised acetylide vibrations ν(C≡C) at 2087 ($\varepsilon \sim 1800$ dm^3 mol^{-1} cm^{-1}) and 2109 cm^{-1} in the high frequency region, whilst **3** only has a single acetylide stretch mode at 2100 cm^{-1}. All assignments are supported by DFT calculations.

The spectrum of $\mathbf{3}^{-\bullet}$ produced by one-electron reduction of **3** in an IR OTTLE cell is given in Fig. S4.† The main IR bands at 1510 cm^{-1}, 1555 cm^{-1} and 1607 cm^{-1} are assigned to the NAP-anion due to the NAP-localised LUMO.

The ultrafast excited state dynamics of **1**, **2** and **3** were investigated by a combination of transient infrared and electronic transient absorption spectroscopies using a 50 fs, 400 nm excitation pulse. Excitation with 400 nm light is expected to populate a singlet excited state manifold of several charge-transfer states, which in **1** and **2** will be of [Ph–C≡C–Pt–C≡C]-to-NAP charge transfer nature (see DFT section). Both TRIR and TA experimental data were analysed using global fit analysis in order to obtain component spectra and related lifetimes for the transient states. The vibrational spectra of the several excited states involved were assigned with the aid of DFT calculations and IR spectroelectrochemistry.

Time-resolved infrared spectroscopy

Fig. 5 shows TRIR spectra for complexes **3**, **1** and **2** (top, middle and bottom, respectively) in CH_2Cl_2 at r.t. at representative delay times after the laser excitation, along with kinetic traces (Fig. 5, bottom) at selected frequencies.

Ultrafast TRIR dynamics in 3, NAP–Pt–Cl. Excitation with 400 nm light leads to an instantaneous loss of ground state absorption (ground state bleach) of the ν(NAP), carbonyl and acetylide bands. An extremely broad transient signal spanning the whole spectrum also appears at early times, and decays with the same lifetime as well-defined transient infrared bands. This signal is assigned to the tail of a very broad transient electronic absorption band of the CT state which extends into the mid-IR region – such behaviour has been previously observed for several Pt(II) acetylides.[48,74]

The well-defined IR transient signals at 1500 cm^{-1}, 1560 cm^{-1} and 1613 cm^{-1} grow in within ≈500 fs and decay with a lifetime of 212 ± 7 ps. These band positions correspond to ν(NAP) and ν(C═O) modes in the reduced form of the NAP–CC– fragment (see IR spectrum of the electrochemically generated $\mathbf{3}^{-\bullet}$, Fig. S4†).[48] In the high frequency region (Fig. 5b) a small signal with a maximum at 2000 cm^{-1} (superimposed upon the broad transient electronic absorption band mentioned above), also decays with a lifetime of 212 ps. This band is attributed to the ν(C≡C) mode in the Pt-to-NAP charge transfer state, shifted to lower energies in comparison to its ground state position due to increased electron density on the antibonding orbital.

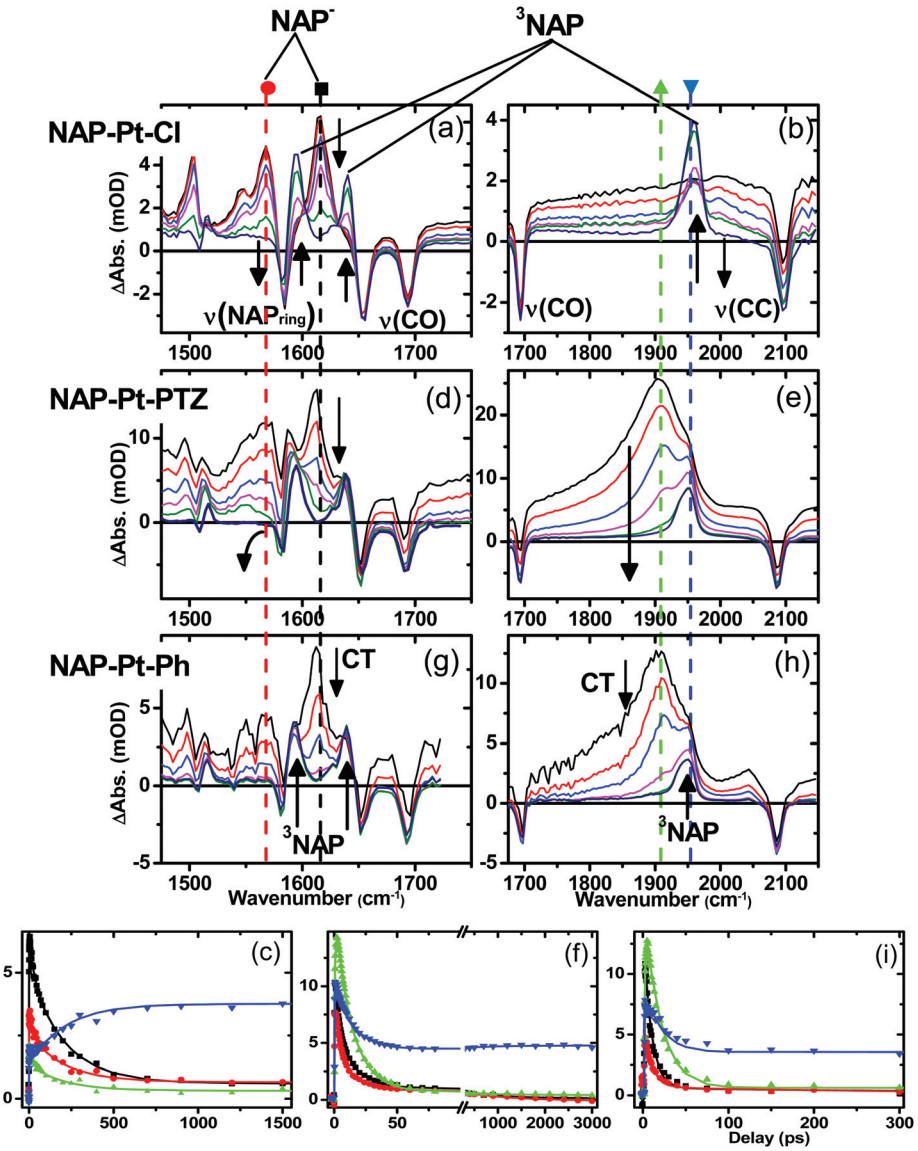

Fig. 5 Time-resolved IR (TRIR) spectra following 400 nm excitation for **3** (NAP–Pt–Cl, a–c), **1** (NAP–Pt–PTZ, d–f) and **2** (NAP–Pt–Ph, g–i) in CH_2Cl_2 and at r.t. The TRIR spectra are shown at representative delay times: 3, 10, 32, 100, 300 and 1200 ps for **3**; 3, 5, 10, 20, 100, and 3000 ps for **1**, and 5, 10, 20, 50, 100 and 200 ps for **2**. The black and red arrows on (d) and (e) represent the major spectral evolution present on all three complexes. The kinetic traces (c, f and i for **3**, **1** and **2**, respectively) are shown for single pixel data at 1613 cm^{-1} (black squares), 1560 cm^{-1} (red circles), 1900 cm^{-1} (green triangles) and 1950 cm^{-1} (blue inverted triangles). The solid lines on the kinetic data were obtained by global fit analysis with instrument response deconvolution. See text for details of the fitting parameters.

The first excited state in **3** that can be detected in the TRIR experiments is assigned primarily to a charge-transfer state manifold involving electron transfer from the metal-acetylide center to the NAP acceptor moiety, hereon referred to as CT. A 1.3 ps component was also extracted from the global analysis and is assigned as an average value for initial excited state evolution following 400 nm excitation; however as IR frequencies are sensitive to charge distribution in the molecules, and the major spectral positions do not evolve on this timescale, it is inferred that there is little or no charge redistribution prior to the 212 ps relaxation. Concomitant with the decay of the CT state, three distinct transient bands at 1590 cm^{-1}, 1640 cm^{-1} and 1950 cm^{-1}, which are characteristic of the ^{3}NAP state,[48] grow in and persist without decay until the 3 ns limit of the setup. The 1590 cm^{-1} band is assigned as a combination of $\nu(C{=}O)_{as}$ and ν(NAP), the 1640 cm^{-1} band as $\nu(C{=}O)_s$ and the 1950 cm^{-1} band as $\nu(C{\equiv}C)$ in the ^{3}NAP state. These assignments concur with the observed ^{3}NAP nature of the lowest excited state obtained from flash photolysis, emission spectroscopy and other studies on analogous compounds.[31,49]

Ultrafast TRIR dynamics in 1 and 2, NAP–Pt–PTZ and NAP–Pt–Ph. A similar process of initial formation of a [Ph–C≡C–Pt–C≡C]-to-NAP charge transfer manifold which ultimately

decays to ^{3}NAP and to the ground state is observed for **1** (Fig. 5d–f) and **2** (Fig. 5g–i). The IR band assignments remain the same as for **3**. In the first 20 ps the decay of the TRIR signal is complex and appears to have contributions from several charge transfer states convolved with their relaxation processes. In the low frequency region, the NAP-anion signal at 1613 cm^{-1} decays in a multiexponential fashion with lifetimes of up to 14 ps for **1** and up to 20 ps for **2**; this decay is concomitant with the formation of ^{3}NAP bands at 1590 and 1640 cm^{-1}. Differently to **2** and **3**, the NAP-anion decay in **1** is accompanied by the appearance of additional bands at 1605 cm^{-1} and 1550 cm^{-1}, with the resulting spectrum strongly resembling that of the NAP-anion in **3**$^{-\bullet}$ and in the CT excited state of **1–3**, but with a slight shift to lower frequencies. This observation indicates the formation of another excited state in **1**, which also incorporates a NAP-anion but has different electron density distribution in other parts of the molecule compared to the precursor CT state. The formation of these two transient bands and associated dynamics (see Fig. 6) are suggestive of electron transfer from the PTZ donor to the oxidised Pt-acetylide centre, forming a full charge-separated state, ^{3}[PTZ$^+$–NAP$^-$], hereon referred to as ^{3}CSS. This ^{3}CSS decays to the ground state with a lifetime of 1.0 ± 0.1 ns. No grow-in of ^{3}NAP bands on nanosecond timescales was observed, setting the upper limit for a ^{3}CSS decay pathway leading to formation of the lower-lying ^{3}NAP to approximately 2%.

In the high frequency region, the ν(C≡C) acetylide stretch signal is different for **1** and **2** compared to **3**, due to the presence of two strongly coupled acetylide groups. A broad, intense transient signal is observed in the TRIR spectra of **1** and **2** between 1710 cm^{-1} and 1910 cm^{-1}, with a maximum at 1908 cm^{-1}, attributed to the CT manifold. The ν(C≡C) band for its successor state ^{3}CSS appears as a small but clearly defined shoulder to the high frequency side of the ground state acetylide bleach (Fig. S5 and S6†), at 2105 cm^{-1}.

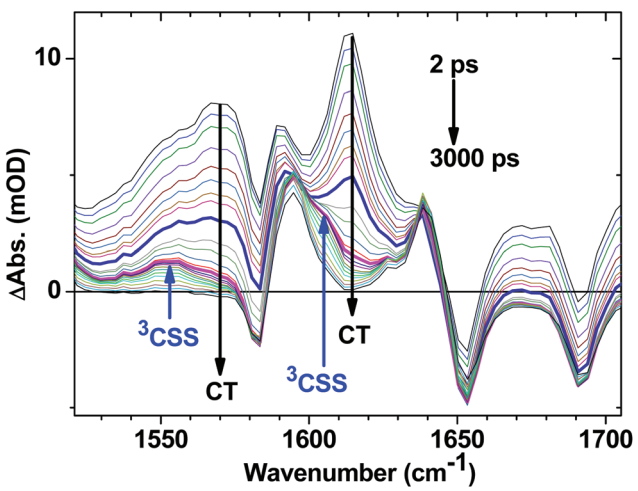

Fig. 6 Expanded fingerprint region of the TRIR data for **1** (Fig. 5d) with delay times spanning from 2 ps to 3 ns following 400 nm, ~50 fs excitation. Arrows indicate the bands associated with the decay of the CT state, and grow in of ^{3}CSS. The highlighted spectra are at delay times of 10 ps (thick blue) and 45 ps (magenta); the latter contains the most pronounced features of ^{3}CSS.

Early time dynamics observed in 1 and 2 with TRIR

A satisfactory fit for the full dynamics of **1** was achieved with a four-exponential function and a constant (representing contribution of ^{3}NAP state which has ~190 μs lifetime and does not decay on the timescale of the ultrafast experiments), with lifetimes of τ_1 = 1.1 ± 0.3 ps, τ_2 = 3.1 ± 1 ps, τ_3 = 14 ± 1 ps (all 3 contributing to the decay of the CT manifold and the formation of ^{3}CSS, ^{3}NAP, and ground state recovery) and τ_4 = 1 ± 0.1 ns (decay of the ^{3}CSS state to the ground state). For **2**, a fit comprising a triple-exponential function and a constant, with τ_1 = 1.0 ± 0.2 ps, τ_2 = 3.2 ± 0.3 ps, and τ_3 = 20 ± 1 ps (all three contributing to the decay of the CT manifold and the formation of ^{3}NAP and ground state recovery) was sufficient.

The UV pump at 400 nm (3.1 eV) contains excess energy compared to the initially populated manifold of CT states. It is therefore expected that electronic evolution within this manifold is convolved with vibrational cooling creating effectively a continuum of processes on the ultrafast time scale. Therefore, the global analysis values obtained in the 1–3 ps range are averaged representations of multiple convoluted ultrafast relaxation processes across the spectrum.

Fig. 7 shows selected kinetic traces plotted at 10 cm^{-1} intervals throughout the broad acetylide signal from 1710 to 1908 cm^{-1} for **1**. The kinetic behaviour across the acetylide IR band is wavenumber-dependent, with the rise and decay times systematically increasing as the energy increases. The fastest component is instrument-limited (instrument response function ≈200 fs), whilst the slowest is 14 ps, which may be assigned to the lifetime of the relaxed, "thermalised", lowest CT state. Structural reorganisation and the fact that the high frequency acetylide mode is anharmonically coupled to surrounding low-frequency vibrationally excited intramolecular modes contributes to the broadening of the band, and to the

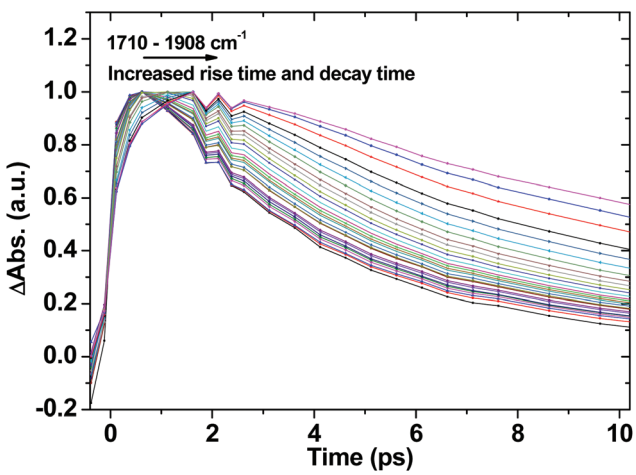

Fig. 7 The initial part of normalised selected TRIR kinetic traces recorded in the range from 1710 cm^{-1} to 1908 cm^{-1} for **1** in CH_2Cl_2 following 400 nm, ~50 fs excitation.

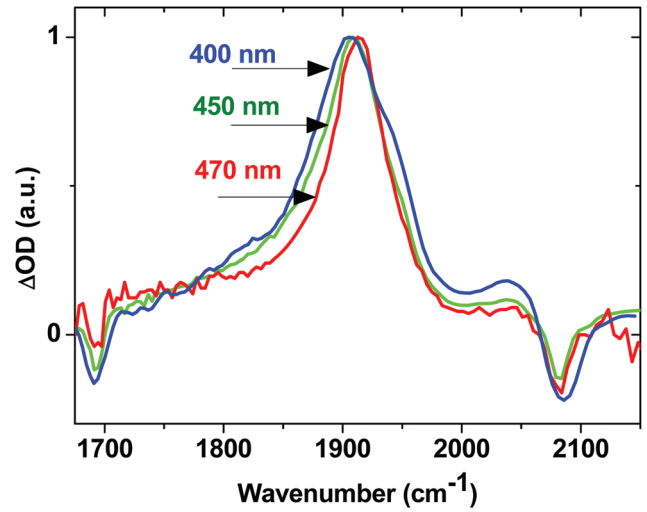

Fig. 8 Normalised TRIR spectra for **2** in CH_2Cl_2, 3 ps after excitation with 400 nm (blue), 450 nm (green) and 470 nm (red) light.

kinetics shown in Fig. 7.[75] Furthermore, the non-exponential ground state recovery and ^{3}NAP formation, which occur with a broad range of timescales matching the lifetime range (≈200 fs–14 ps) of the broad IR transient band, is evidence of electron transfer (ET) occurring from non-thermalised excited states.[76,77] Vibrational-electronic (vibronic) interactions in these systems are therefore expected to play an important role in ET rates.[1,78–80]

The effect of excess excitation energy on excited state dynamics was further investigated using different pump wavelengths. Fig. 8 shows the TRIR signal for **2** in the acetylide region 3 ps after initial excitation at 400 nm (3.10 eV, blue line), 450 nm (2.76 eV, green line) and 470 nm (2.64 eV, red line), all within the ML/L′CT absorption manifold. Using progressively longer wavelength excitation pulse (*i.e.*, photons of lower energy) results in the narrowing, and some blue-shift, of the dominant ν(C≡C) band. There is also no evidence of the near-instantaneous population of the ^{3}NAP state when exciting with energies lower than 400 nm as the characteristic shoulder at 1950 cm^{-1} (Fig. 8, blue) is not observed in the experiment under 470 nm excitation (Fig. 8, red). ^{3}NAP formation is therefore accelerated in the presence of excess energy in its precursor states. Importantly, whilst the ET dynamics are affected by the excitation wavelength, the yield of the final ^{3}NAP state in **1–3** ultimately remains unchanged, as determined by the constant phosphorescence yield observed in steady-state emission spectroscopy under excitation ranging from 360 to 470 nm. This indicates that ET rates are uniformly accelerated across all three pathways in the presence of excess energy.

Estimation of the yields of product states for 1 – target analysis

The initial CT manifold in **1** (main IR bands at 1560, 1613 and 1908 cm^{-1}) decays over three separate electron transfer pathways: (i) forward ET to form the full ^{3}CSS, ^{3}[PTZ$^+$–NAP$^-$] (1550, 1605, 2105 cm^{-1}), and charge recombination to form either (ii) the intraligand triplet ^{3}NAP (1590, 1640, 1950 cm^{-1}) or (iii) the ground state. Since the lifetimes of the states involved differ by several orders of magnitude from one another, it is possible to use target analysis to determine the ideal branching model that will accurately reproduce the concentration profile of the ground state recovery. Fig. 9a shows the model assumed for **1**, which takes into account electron transfer from non-thermalized excited states, including instrument-limited processes occurring in less than 200 fs, evident in the ultrafast recovery of the ground state (Fig. 9b inset) and ^{3}NAP formation (Fig. 6) observed in the data. The ^{3}NAP yield is fixed to that estimated by singlet oxygen yield measurements (57%), and the ^{3}CSS and ground state yields are varied with 2% intervals between 4–16% and 39–27%, respectively.

Fig. 9b plots the calculated ground state concentration profiles for all modelled branching parameters, and compares the outputs with the ground state bleach recovery extracted from the TRIR data at 1690 cm^{-1}, *i.e.* the ν(C═O) band free of any overlapping transient (the broad offset is subtracted as background for this analysis). The best fit to the data is the green line, where the branching parameters are 10%, 33% and 57% to the ^{3}CSS, ground state and ^{3}NAP, respectively. From this analysis, the yield of the ^{3}CSS is estimated as 10 ± 2%. The resulting concentration profile for all modelled states is shown in Fig. 9c; additional detail are given in Fig. S7.†

Ultrafast transient absorption spectroscopy

Ultrafast electronic transient absorption spectroscopy data for **1**, **2** and **3** in CH_2Cl_2 are shown in Fig. 10. Three prominent features are common to all compounds over femto- to nanosecond timescale: the transient band around 460 nm assigned to the NAP anion in CT state(s) and partially overlapped with the ground state bleach; stimulated emission giving rise to the negative going features in the range 480–600 nm; and at late time-delays a broad feature which corresponds well to the ^{3}NAP spectra obtained by nanosecond flash photolysis. The positions of the stimulated emission correspond to that obtained from steady-state emission spectroscopy (*ca.* 500 nm, Table 2) assigned to charge-transfer-to-NAP excited states. Stimulated emission obscures any absorption bands that may occur in its spectral region.

In **3**, electronic state evolution and excess energy dissipation immediately following the 50 fs, 400 nm excitation is reflected in the initial spectral dynamics appearing as changes in the 480 nm-region and grow-in of stimulated emission at 520 nm (τ_1 = 0.9 ± 0.3 ps). Such spectral evolution at early times is similar in all three compounds (see decay associated spectra in Fig. S8–S10†). Following this initial evolution, in the transient spectra of **3** the stimulated emission at 520 nm and the main transient feature centred at 460 nm decay uniformly with the formation of ^{3}NAP with τ_2 = 206 ± 5 ps, which matches well the 212 ± 7 ps lifetime obtained for this process from TRIR.

For **1** and **2**, the position of the stimulated emission signal evolves with time, decreasing progressively in energy over tens of picoseconds. This is consistent with stimulated emission taking place from a continuum of vibronic states:

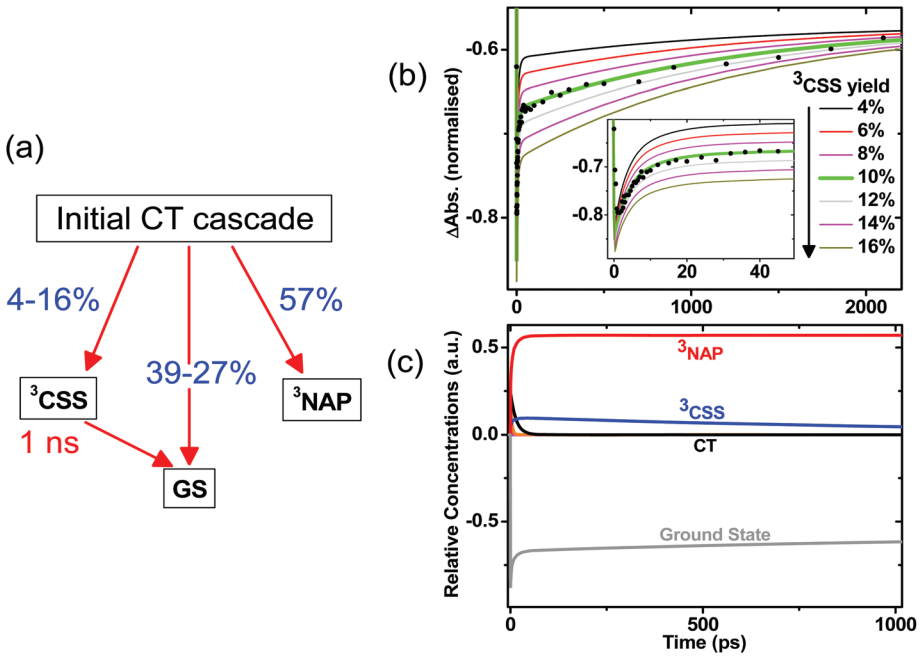

Fig. 9 (a) Model used in target analysis of **1**, where the branching ratio between the charge separated state ^{3}CSS and GS from the initial excited states is varied. The four components used to model the ultrafast CT cascade and reproduce the dynamics satisfactorily are 0.2, 1.1, 3.2 and 14 ps. (b) Calculated concentration profiles of the ground state as a function of time for different branching parameters. The ground state ν(C=O) bleach at 1690 cm^{-1} from the TRIR data is plotted for comparison (black circles). The best fit achieved is with 10% ^{3}CSS and 33% GS yields, highlighted in green. Inset: early-time data. (c) Calculated concentration profiles of all modelled states up to 1 ns with a ^{3}CSS yield of 10% and GS yield of 33%.

higher-energy emission occurs at early times as higher-lying states are populated soon after the UV pump; the emission energy then decreases as electronic state evolution, IVR and solvent equilibration take place. Therefore, as in the TRIR analysis above, the lifetimes obtained from global analysis for the earliest events (<3 ps) do not necessarily represent discrete excited states, but should be considered an ensemble average of the initial concomitant charge transfer and cooling processes which lead to continuously evolving multi-exponential kinetics.

The overall dynamics of **2** (Fig. 10f) were modelled satisfactorily using τ_1 = 0.6 ± 0.3 ps, τ_2 = 2.2 ± 0.6 ps, τ_3 = 19 ± 2 ps and a constant representing ^{3}NAP contribution; a minor component decay of τ_4 = 160 ± 30 ps was also required for the fit; this component was not reliably extracted from TRIR analysis. In **2**, following initial evolution represented by τ_1 and τ_2, stimulated emission and the band at 470 nm decay with 19 ± 2 ps, concurring with the 20 ± 1 ps lifetime obtained for these processes from TRIR measurements.

In the DBA triad **1**, the overall dynamics (Fig. 10d) can be satisfactorily modelled using τ_1 = 0.5 ± 0.3 ps, τ_2 = 1.8 ± 0.3 ps, τ_3 = 13 ± 1 ps, τ_4 = 800 ± 200 ps and a constant. Stimulated emission has fully decayed by 60 ps (with major components τ_2 = 1.8 ps and τ_3 = 13 ± 1 ps), by which time the presence of an additional intermediate state (τ_4 = 800 ± 200 ps) overlapped with ^{3}NAP is clearly evident by small additional transient bands at 516 nm and 565 nm, not detected in the spectra of **2** or **3**. From TRIR studies we expect this state to be the full charge separated state, ^{3}[PTZ$^+$–NAP$^-$]. Due to overlap of the UV-Vis absorption bands for the ground state, NAP anion, PTZ cation and ^{3}NAP, as well as the relatively low yield of the ^{3}CSS state, this state is not strongly pronounced in the TA data. However, the very different timescales over which these overlapping electronic states decay allow us to deconvolve the pure spectrum of the intermediate state from other electronic states: the spectrum of the intermediate state can be simply obtained by subtracting the 3 ns spectrum (^{3}NAP spectrum) from that at 60 ps, or extracting the 800 ps lifetime spectrum from the DAS resulting from global analysis (Fig. S9†).

In order to ascertain the absorption features of NAP–CC-anion and PTZ-cation anticipated in the full charge-separated ^{3}[PTZ$^+$–NAP$^-$] state of **1**, UV/Vis spectroelectrochemical studies were performed on model compounds **3** and **4** (Fig. 11b). The spectrum of **3**$^{-\bullet}$ obtained upon one-electron reduction of **3** displays NAP-anion absorbances at 460, 525 and 565 nm (Fig. 11b, black spectrum). The spectrum of **4**$^{+\bullet}$ obtained as a result of one-electron oxidation of **4** displays absorption bands attributed to PTZ-cation at 516 nm (Fig. 11b, blue spectrum). Comparison of the transient absorption spectrum of the intermediate state (at 60 ps) of **1** with the spectra of the electrochemically generated radical ion species clearly show that the PTZ cation band at 516 nm and the NAP-anion band at 565 nm are observed. Thus the spectral profile of the intermediate state matches that expected for the full charge separated state ^{3}[PTZ$^+$–NAP$^-$], a result that concurs with the assignment from TRIR analysis.

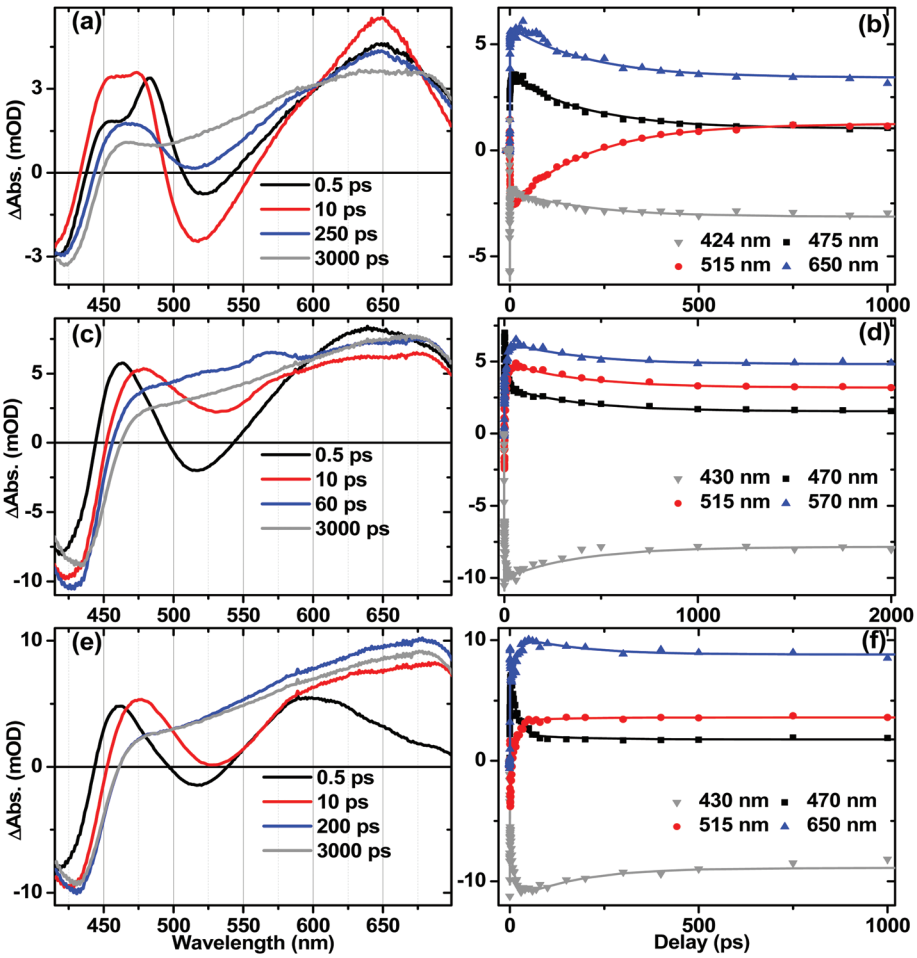

Fig. 10 Representative UV-Visible transient absorption spectra and corresponding kinetics following 400 nm excitation for **3**, NAP–Pt–Cl (a, b); **1**, NAP–Pt–PTZ (c, d); and **2**, NAP–Pt–Ph (e, f), in CH_2Cl_2 and at r.t. Solid lines on kinetic traces are the results of global analysis with instrument response deconvolution. See text for details of the fitting parameters.

The photophysical pictures obtained from the TA and TRIR measurements are mutually consistent, and indicate that excitation of the DBA triad **1** with 400 nm light populates a manifold of CT states that decay over three electron transfer pathways, with the formation of a full CSS, ^{3}NAP-state, and reformation of the ground state.

Density functional theory (DFT)

DFT calculations have been performed for **1–3**, the $-C_8H_{17}$ group was replaced by $-C_2H_5$, and the butyl chains by methyl groups for computational efficiency. The correctness of this assumption was tested for **2** (Fig. S12†); the calculated IR spectra display almost identical positions for the major IR bands regardless of whether C_8H_{17}, CH_3, C_2H_5, or butyl was used, showing that such replacements are not crucial to our understanding of the properties of these compounds.

Fig. S13a† demonstrates a very good agreement between the calculated and the experimental FTIR spectra of **1** in CH_2Cl_2. Analysis of the bands confirms the assignments made above from the experimental data: the peaks at 1583 cm^{-1}, 1653 cm^{-1}, 1692 cm^{-1} are predominantly the NAP ring stretch mode and carbonyl modes (antisymmetric and symmetric), respectively; the peak at 2087 cm^{-1} with a shoulder at 2109 cm^{-1} is due to antisymmetric and symmetric combinations of the acetylide stretching vibrations. Other minor bands in the region shown are due to ring stretch and bending modes on the NAP, Phenyl or PTZ fragments. A very good agreement between the late-time experimental TRIR spectrum and the calculated TRIR spectrum (obtained by subtracting singlet ground state spectrum from the spectrum of the lowest triplet state using the scaling factors for the singlet ground state), allows us to assign the IR bands conclusively (Fig. S13b†).

Using the optimized structures for both ground singlet and triplet states, the electronic absorption spectra of both states were obtained using time-dependent DFT (TD-DFT). The resultant singlet UV-Vis spectra together with simulated TA spectra are given in Fig. S14.† The major transitions for **1** are summarized in Table 3, and the molecular orbitals involved in these transitions presented in Fig. 12. The calculations show that the absorption band centered at 430 nm in **1** comprises several transitions from the orbitals delocalized over the

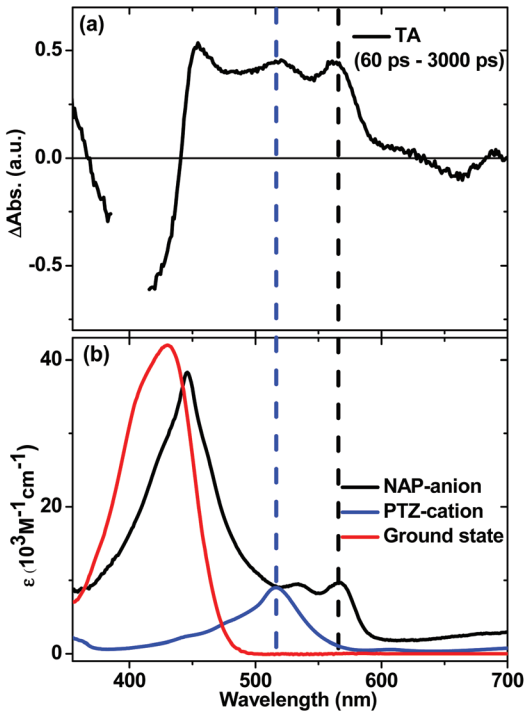

Fig. 11 (a) Transient absorption spectrum of the intermediate state, ^{3}[PTZ$^+$–NAP$^-$], free from contributions of the initial CT state and the ^{3}NAP-state (obtained by subtracting the ^{3}NAP spectrum from the transient absorption spectrum at 60 ps). The data points around 400 nm are omitted due to strong scattering of the excitation pulse in this region. (b) UV-Vis absorption spectra of electrochemically generated radical-anion **3**$^{-\bullet}$ containing the NAP-anion (black, at 243 K), and radical-cation **4**$^{+\bullet}$ containing the PTZ-cation (blue, at 243 K), overlapped with the spectrum of the ground state of **1** (red).

Table 3 Results of TD-DFT calculations of the electronic absorption spectrum for **1** showing the contribution of major transitions to the lowest energy absorption band centered at 430 nm (transitions with oscillator strengths above 0.04 are shown; 100 states in calculation)

Transition	Wavelength (nm)	Osc. strength	Major contribs
1	463.316	0.1204	H−1 → LUMO (56%) HOMO → LUMO (38%)
3	439.876	0.2276	H−3 → LUMO (10%); H−2 → LUMO (78%)
4	406.117	0.3257	H−3 → LUMO (82%); H−2 → LUMO (14%)

central bridge C≡C–Pt–C≡C–Ph (HOMO−3, HOMO−2 and HOMO−1) to the NAP-localized LUMO. TD-DFT calculations for **2** confirm that these transitions arise primarily from the same orbitals (Fig. S17, Table S5†). This result agrees well with the nearly identical experimental UV/Vis spectra (Fig. 2) for **1** and **2** in the 430 nm region.

The nature of the multiple excited states involved can be further elucidated by electrostatic potential (ESP) maps for the singlet and triplet states of **1**, Fig. 13. To simplify the discussion, only a few discreet excited states in the singlet and triplet manifolds are analysed here. This is a simplification given the strong spin–orbit coupling and the large number of excited states in both singlet and triplet manifolds that are involved in the excited state evolution; a more accurate representation requires the inclusion of spin–orbit coupling in the calculations to model the singlet/triplet mixing expected in such systems. This is however computationally prohibitively expensive for such large transition metal complexes.

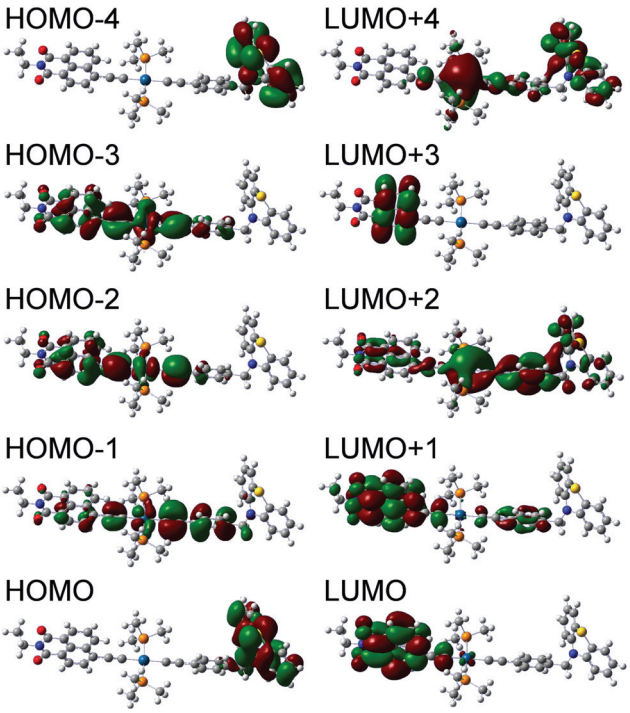

Fig. 12 Orbitals involved in the major electronic transitions of **1** (see Table 3).

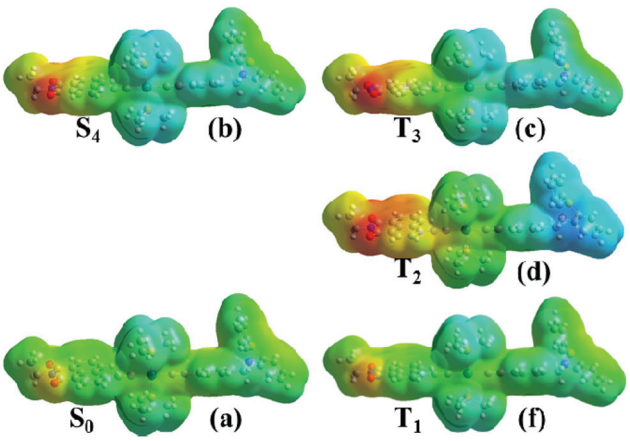

Fig. 13 Electron density maps calculated for the initially populated singlet ground state (S_0, a), singlet excited state (S_4, b), second triplet excited state (T_3, c), first triplet excited state (T_2, d) and lowest triplet state (T_1, e) for **1** in CH_2Cl_2. Colors correspond to charges with red being −0.1 and blue being +0.1.

The singlet excited state populated with the 400 nm pulse used in the pump-probe experiments was assumed to correspond to the 4th transition from Table 3 due to its proximity to the pulse energy as well as its large oscillator strength. This state is populated instantaneously, and therefore singlet ground state geometry is preserved. It is further assumed that CT states of triplet character are populated on an ultrafast timescale and thus the initial triplet excited state T_3 will still retain the geometry of the singlet ground state. T_2 is a full charge separated state ^{3}CSS with 1 ns lifetime (*vide supra*) and is populated over several picoseconds, and therefore its geometry is likely to be different from that of T_3. The structure for T_2 was thus optimized starting from the triplet ground state structure, T_1. It is clear from comparing panels (a) and (b) that the initial excitation ($S_0 \rightarrow S_4$) induces electron transfer primarily from the central bridge, [≡Pt(PBu$_3$)$_2$≡Ph] to the NAP moiety. These potentials do not change significantly in the second step of the process, $S_4 \rightarrow T_3$ (comparing panel (b) and (c) from Fig. 13). After this the process may evolve into full charge separation when the hole transfers to the PTZ donor, as shown by the electrostatic density map of panel (d) for the first triplet excited state, T_2. The lowest triplet state T_1 resembles the singlet ground state in terms of electrostatic density, which concurs with its assignment as an intraligand excited state. Thus the nature of the ESPs of the excited states as obtained from our calculations agrees well with assignments inferred from spectroscopic data.

Summary of the excited state processes

The above results can be summarized as follows. In all three NAP-containing complexes **1–3**, the 400 nm, ~50 fs excitation pulse populates a manifold of charge-transfer states involving electron transfer from the Pt-acetylide centre to the NAP acceptor. The identical absorption maxima for **1** and **2**, which are only slightly different compared to the Cl precursor **3**, and the absence of any >350 nm absorbances in the NAP-free building block **4**, confirm the lack of PTZ involvement in the initial excitation event. The early time dynamics in **1–2** immediately following excitation involve several electronic excited states, which due to the ultrafast nature of the processes involved are vibrationally hot, and therefore electronic relaxation is convolved with intramolecular vibrational redistribution, internal conversion, solvent relaxation, and intersystem crossing. Following an initial ultrafast electronic evolution on the 0.5–1 ps timescale, strong stimulated emission is observed at the same spectral position as that assigned to the emission from a [Ph–C≡C–Pt–C≡C]-to-NAP charge transfer excited state in the steady-state emission spectra. Its estimated radiative lifetime of 8–14 ns is somewhat longer than the 1–2 ns anticipated for pure spin allowed transitions, but significantly shorter than those expected for spin-forbidden transitions.[81] The decay of the stimulated emission is multiexponential, and is accompanied by the formation of triplet states and recovery of the singlet ground state. Intersystem crossing in **1–3** is expected to occur on ultrafast timescales due to strong spin–orbit coupling promoted by the heavy-atom effect of the Pt centre, and indeed we observe the instantaneous rise of ^{3}NAP signals in the transient spectra immediately following excitation. Pt(II) complexes are reported to have ISC rates ranging from 70 ± 40 fs, measured by fluorescence upconversion in a close analogue of **1** and **2**, Ph–CC–Pt(PBu$_3$)$_2$–CC–Ph, to hundreds of picoseconds.[36,43,81–85] Direct population of the triplet NAP *via* a direct ligand-localised excitation which would lead to slower ISC rates[86] is highly unlikely as this ligand is coupled to the Pt centre through the rigid acetylide linker. It has been established that ISC rates in transition metal complexes, in addition to spin–orbit coupling, are influenced by the energy difference between the singlet and triplet states involved, by the degree of metal orbital contribution, and other factors such as transient distortion along the reaction coordinate promoting ISC.[81,87–90] In **1**, excitation with 400 nm light populates a manifold of S_1–S_4 singlet states, all of charge-transfer character and all within a 0.4 eV energy range. The energies, geometries and electron density distribution in the triplet states T_3–T_5 match closely to the singlet manifold, satisfying the requirements for efficient ISC. Thus, in the model assuming pure spin states, the triad **1** has a pool of nearly iso-energetic charge-transfer excited states, including at least three singlets and three triplets. Strong mixing[81,91] of these states is highly likely, and may account for the simultaneous observation of an intense stimulated emission and ultrafast formation of ^{3}NAP (the lowest triplet state which is widely separated in energy from the rest of the triplet manifold). Thus, the early time dynamics in **1** are assumed to proceed through a cascade of spin–orbit states, a behaviour similar to that reported for several other transition metal complexes.[89,92,93]

Using the transient absorption and infrared spectroscopic data, and extracting energy levels of the electronic states from cyclic voltammetry and emission data, one can construct an energy level diagram for **1** as presented in Fig. 14.

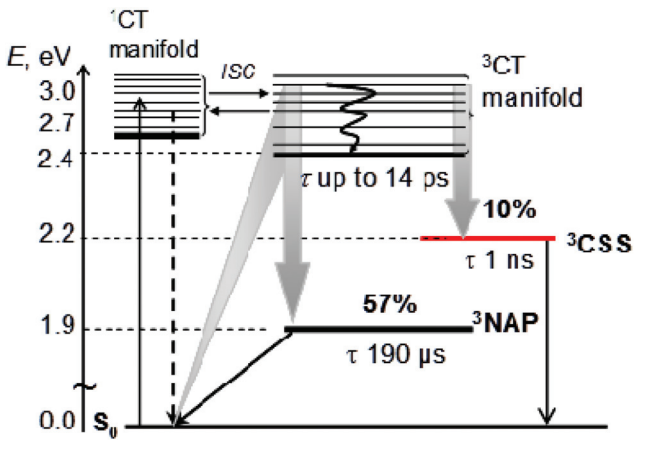

Fig. 14 Summary of electronic transitions and excited state lifetimes for **1**, NAP–Pt–PTZ, following 400 nm excitation in CH_2Cl_2 at r.t. The energy values are derived from absorption, emission and cyclic voltammetry data. Electron transfer from the CT manifold occurs from non-thermalized states. The % relative yields of product states are indicated.

Upon excitation of **1–3** with ~50 fs, 400 nm light, a manifold of charge transfer states is populated where electron density is shifted from the central Pt-containing bridge to the NAP moiety. The initially formed CT excited state branches along three concurrent decay pathways: back electron transfer leading to ground state recovery and ^{3}NAP-state formation (57% yield), and forward electron transfer from the PTZ-unit leading to complete charge separation with the formation of the [NAP$^-$–PTZ$^+$] full charge-separated state, ^{3}CSS (10% yield, 1 ns lifetime). The yields of product states were obtained using singlet oxygen yield measurements, target analysis and ground state bleach recovery dynamics from the TRIR data.

Conclusions

This study contributes to our understanding of the rich photophysics of Pt(II) *trans*-acetylide donor–acceptor systems by presenting an asymmetric donor–bridge-acceptor triad containing NAP as an electron acceptor and phenothiazine as an electron donor, NAP≡Pt(PBu$_3$)$_2$≡Ph–CH$_2$–PTZ (**1**). Its photophysical properties were extensively characterized by electronic and vibrational spectroscopies on timescales ranging from ~100 fs to milliseconds. The comparison with the photophysical behavior of the constituent "building blocks" **2–4**, along with the results of UV/Vis/IR spectroelectrochemical studies and DFT calculations, assisted in assigning the nature of several excited states involved, as well as in elucidating the complex excited states dynamics and pathways in **1**. The initial excitation of **1** with visible light leads to the formation of a manifold of charge-transfer states where electron density shifts from the Pt-acetylide bridge to the NAP acceptor. This charge-transfer manifold undergoes excited state branching on the ultrafast (0.2–14 ps) timescale over three pathways to form a long-lived (190 μs) acceptor-localized triplet state, to recombine back to the ground state, and to engage in forward electron transfer with the formation of the full charge-separated state. Thus the ultrafast formation of a full CSS in **1** has been established where the distance between the charges is ~18 Å. The DBA molecular triad **1** displays intriguing dynamics where ultrafast electron transfer occurs from a manifold of non-thermalized charge transfer excited states. This direct observation may be of importance to other transition metal complexes utilised in light-harvesting and molecular electronics. Such studies are directly related to building efficient artificial systems which emulate natural photosynthesis and undergo rapid and efficient energy and electron transfer over significant distances.

Experimental section

Synthesis

Synthesis of 4-bromo-*N*-octyl-1,8-naphthalimide, 4-ethynyl-*N*-octyl-1,8-naphthalimide, *N*-(4-ethynylbenzyl)-phenothiazine, and *cis*-Pt(P^{n}Bu$_3$)$_2$Cl$_2$ are given in the ESI.†

***trans*-(4-Ethynyl-*N*-octyl-1,8-naphthalimide)Pt(PBu$_3$)$_2$Cl (3).** 4-Ethynyl-*N*-octyl-1,8-naphthalimide (141 mg, 0.42 mmol) was dissolved in ^{i}Pr$_2$NH (40 ml) and deaerated with bubbling Ar for 15 min. *cis*-Pt(P^{n}Bu$_3$)$_2$Cl$_2$ (394 mg, 0.58 mmol) was added and the reaction mixture heated to 90 °C in the dark for 16 h. Cooling to room temperature followed by evaporation of the solvent gave a dark orange residue which was subsequently purified by column chromatography (SiO$_2$, CH$_2$Cl$_2$). The product eluted as the first major yellow coloured band, with a second band of yellow coloured material being found to contain a small quantity of the bis substituted complex. Removal of the solvent from the first fraction gave the product as a bright yellow oil. Yield 186 mg (0.19 mmol, 45%). ^{1}H NMR (CDCl$_3$): 0.83–0.93 (m, 21H), 1.20–1.47 (m, 22H), 1.53–1.65 (m, 12H), 1.66–1.76 (m, 2H), 1.92–2.08 (m, 12H), 4.15 (t, J = 7.60 Hz, 2H), 7.58 (d, J = 7.72 Hz, 1H), 7.67 (t, J = 7.40 Hz, 1H), 8.44 (d, J = 7.72 Hz, 1H), 8.57 (dd, J = 1.08, 7.28 Hz, 1H), 8.72 (dd, J = 1.08, 8.32 Hz, 1H). ^{31}P NMR (CDCl$_3$): 7.79 (J_{Pt-P} = 2338 Hz). AP-MS: m/z = 967.5 (M$^+$, 100%).

***trans*-(4-Ethynyl-*N*-octyl-1,8-naphthalimide)(ethynylbenzene)-Pt(PBu$_3$)$_2$ (2).** ^{i}Pr$_2$NH (20 ml) was deaerated by bubbling Ar for 15 min and transferred to a reaction vessel containing **3** (150 mg, 0.15 mmol) and CuI (15 mg, 0.078 mmol). Phenylacetylene (60 μl, ρ 0.93 g ml^{-1}, 0.54 mmol) was added and the reaction mixture stirred in the dark at 40 °C for 42 h. Removal of the solvent yielded a dark orange coloured residue which was subsequently purified by column chromatography (SiO$_2$, CH$_2$Cl$_2$). The product was obtained from the first of two yellow coloured bands. Yield 102 mg (0.098 mmol, 64%). ^{1}H NMR (CDCl$_3$): 0.83–0.94 (m, 21H), 1.21–1.48 (m, 22H), 1.57–1.68 (m, 12H), 1.68–1.76 (m, 2H), 2.05–2.21 (m, 12H), 4.15 (t, J = 7.60 Hz, 2H), 7.13 (tt, J = 1.32, 7.32 Hz, 1H), 7.22 (t, J = 7.28 Hz, 2H), 7.28 (dd, J = 1.40, 8.24 Hz, 2H), 7.60 (d, J = 7.72 Hz, 1H), 7.66 (t, J = 7.80 Hz, 1H), 8.44 (d, J = 7.72 Hz, 1H), 8.56 (dd, J = 1.16, 7.20 Hz, 1H), 8.78 (dd, J = 1.16, 8.36 Hz, 1H). ^{31}P NMR (CDCl$_3$): 3.89 (J_{Pt-P} = 2336 Hz). MALDI-MS: m/z 1032.8 (M$^+$).

***trans*-(4-Ethynyl-*N*-octyl-1,8-naphthalimide)(*N*-(4-ethynylbenzyl)-phenothiazine)Pt(PBu$_3$)$_2$ (1).** *N*-(4-Ethynylbenzyl)-phenothiazine (105 mg, 0.33 mmol) was dissolved in ^{i}Pr$_2$NH (25 ml) and deaerated with bubbling Ar for 15 min. The solution was then transferred to a reaction vessel containing **3** (112 mg, 0.11 mmol) and CuI (6 mg, 0.031 mmol). The reaction mixture was stirred at 35 °C in the dark for 30 h. The solvent was removed and the crude residue purified by column chromatography (SiO$_2$, 1 : 9 hexane–CH$_2$Cl$_2$). The product eluted as the first of two yellow/orange coloured bands, with removal of the solvent yielding the bright yellow title complex. Yield = 64 mg (0.051 mmol, 44%). ^{1}H NMR (CDCl$_3$): 0.84–0.92 (m, 21H), 1.20–1.47 (m, 22H), 1.58–1.67 (m, 12H), 1.67–1.76 (m, 2H), 2.05–2.20 (m, 12H), 4.15 (t, J = 7.64 Hz, 2H), 5.03 (s, 2H), 6.63 (d, J = 8.16 Hz, 2H), 6.85 (td, J = 0.88, 7.44 Hz, 2H), 6.97 (td, J = 1.48, 7.86 Hz, 2H), 7.07 (dd, J = 1.48, 7.56 Hz, 2H), 7.15 (d, J = 8.20 Hz, 2H), 7.24 (d, J = 8.20 Hz, 2H), 7.59 (d, J = 7.76 Hz, 1H), 7.66 (t, J = 7.84 Hz, 1H), 8.44 (d, J = 7.72 Hz, 1H), 8.56 (dd, J = 0.92, 7.24 Hz, 1H), 8.77 (dd, J = 0.96, 8.28 Hz, 1H). ^{31}P NMR (CDCl$_3$): 3.80 (J_{Pt-P} = 2332 Hz). AP-MS: 1244.5 (M$^+$).

***trans*-{*N*-(4-Ethynylbenzyl)-phenothiazine}Pt(PBu_3)$_2$Cl (4).** *N*-(4-Ethynylbenzyl)-phenothiazine (35 mg, 0.11 mmol) and *cis*-Pt(P^nBu_3)Cl_2 (94 mg, 0.14 mmol) were dissolved in degassed $^iPr_2NH$ (15 ml) and heated to 60 °C in the dark for 22 h. The reaction mixture was allowed to cool to r.t. and the solvent removed to leave a pale yellow oily residue which was subsequently purified *via* column chromatography (SiO_2, 2 : 3 CH_2Cl_2–hexane). The product was initially obtained as a clear oil, which after thorough drying *in vacuo* afforded a white solid. Yield = 37 mg (0.039 mmol, 36%) ^{1}H NMR ($CDCl_3$): 0.91 (t, J = 7.24 Hz, 18H), 1.38–1.49 (m, 12H), 1.50–1.61 (m, 12H), 1.93–2.07 (m, 12H), 5.01 (s, 2H), 6.62 (dd, J = 0.84, 8.12 Hz, 2H), 6.85 (td, J = 1.08, 7.44 Hz, 2H), 6.96 (td, J = 1.52, 7.84 Hz, 2H), 7.07 (dd, J = 1.52, 7.56 Hz, 2H), 7.13 (d, J = 8.28 Hz, 2H), 7.19 (d, J = 8.24 Hz, 2H). ^{31}P NMR ($CDCl_3$): 6.80 (J_{Pt-P} = 2374 Hz). MALDI-MS: m/z = 946.5 (M^+), 749.4 (M^+ − PTZ).

Equipment

UV/vis spectroscopy studies were carried out using a Cary-50 Bio spectrophotometer. Emission spectroscopy studies were carried out with a Fluoromax-4 spectrofluorometer. Luminescence lifetimes were measured with a Mini-τ fluorimeter (Edinburgh Instruments) containing a picosecond diode laser (410 nm, 80 ps) as an excitation source. Experimental uncertainties are estimated as 20% for emission quantum yields and 15% for the lifetimes. Solutions of the complexes were degassed in quartz cells with 3× freeze–pump–thaw cycles unless otherwise stated. The UV-Vis absorption spectra were regularly checked for stability during the experiments.

Nanosecond Flash Photolysis studies were conducted on a home-built setup based on a tuneable Ti:Sapph laser, time resolution *ca.* 25 ns.

Picosecond TRIR studies were performed in the Ultrafast Spectroscopy Laboratory, Rutherford Appleton Laboratory, UK, ULTRA[94] facility. The IR spectrometer comprised two synchronized 10 kHz, 8 W, 40 fs and 2 ps Ti:Sapph oscillator/regenerative amplifiers (Thales) which pump a range of optical parametric amplifiers (TOPAS). A portion of the 40 fs Ti:Sapph beam was used to generate tuneable mid-IR probe light with *ca.* 400 cm^{-1} bandwidth. The instrumental response function for TRIR measurements is approx. 250 fs. The probe and pump beam diameters at the sample were *ca.* 70 and 120 μm, resp., the pump energy at the sample was 1 to 1.5 μJ. Changes in IR absorption spectra were recorded by three HgCdTe linear-IR array detectors on a shot-by-shot basis. All experiments were carried out in Harrick cells with 2 mm thick CaF_2 windows and 500 to 950 μm path length; typical optical density of 0.5 to 1 at 400 nm. All samples were mounted on a 2D-raster stage and solutions were flowed to ensure photostability.

Femtosecond TA experiments were performed at ULTRA[94] facility (data shown in the text) and at the B. I. Stepanov Institute of Physics, Minsk[95,96] (not shown). The data obtained on both setups are in good qualitative agreement. The details are given in the ESI.†

Analysis of ultrafast time-resolved data was performed using the open-source software Glotaran v1.3.[97] A combination of Singular Value Decomposition (SVD), global and target analysis was used to extract kinetic rate constants and associated spectral contributions for each system. Full descriptions of these methods can be found elsewhere.[87,97–99] More details on the results of this analysis can be found in the ESI.†

DFT

All calculations were performed using Gaussian 09, version C.01,[100] compiled using Portland compiler v 8.0–2 with the Gaussian-supplied versions of ATLAS and BLAS,[101] using the B3LYP functional of DFT.[102] In all cases an extensive basis set was used, consisting of 6-311G**[103] on all elements apart from Pt, which was described using a Stuttgart–Dresden pseudopotential.[104] Previous work shown that this approach results in a reasonably accurate description of transition-metal complexes and their properties,[14,105] allowing for semi-quantitative comparison with experiments. Our calculations on **1** used 1212 basis functions for 394 electrons. The bulk solvent was described using PCM,[106] with the standard parameters for CH_2Cl_2 as supplied by Gaussian. All integrals were done ultrafine.

Acknowledgements

We thank the EPSRC, E-Futures DTC, the University of Sheffield, the STFC (access to beam time at the Lasers for Science Facility), and the Royal Society for financial support, and Dr P Portius for collaboration. All calculations were performed on the "Jupiter" cluster of the Theoretical Chemistry Group of the University of Sheffield.

References

1 P. F. Barbara, T. J. Meyer and M. A. Ratner, *J. Phys. Chem.*, 1996, **100**, 13148–13168.
2 J. H. Alstrum-Acevedo, M. K. Brennaman and T. J. Meyer, *Inorg. Chem.*, 2005, **44**, 6802–6827.
3 R. Eisenberg, *Science*, 2009, **324**, 44–45.
4 D. Hanss, M. E. Walther and O. S. Wenger, *Coord. Chem. Rev.*, 2010, **254**, 2584–2592.
5 G. A. Parada, L. A. Fredin, M. Santoni, R. Lomoth, O. Johansson, P. Persson and S. Ott, *Inorg. Chem.*, 2013, **52**, 5128–5137.
6 E. C.-H. Kwok, M.-Y. Chan, K. M.-C. Wong and V. W.-W. Yam, *Chem. – Eur. J.*, 2014, **20**, 3142–3153.
7 B. Ventura, A. Barbieri, A. Zanelli, F. Barigelletti, J. B. Seneclauze, S. Diring and R. Ziessel, *Inorg. Chem.*, 2009, **48**, 6409–6416.
8 A. Barbieri, B. Ventura and R. Ziessel, *Coord. Chem. Rev.*, 2012, **256**, 1732–1741.
9 A. Vacher, F. Barrière, F. Camerel, J.-F. Bergamini, T. Roisnel and D. Lorcy, *Dalton Trans.*, 2013, **42**, 383–394.

10 P. Jarosz, J. Thall, J. Schneider, D. Kumaresan, R. Schmehl and R. Eisenberg, *Energy Environ. Sci.*, 2008, **1**, 573–583.
11 N. Damrauer, G. Cerullo, A. Yeh, T. Boussie, C. Shank and J. McCusker, *Science*, 1997, **275**, 54–57.
12 J. M. Butler, M. W. George, J. R. Schoonover, D. M. Dattelbaum and T. J. Meyer, *Coord. Chem. Rev.*, 2007, **251**, 492–514.
13 E. A. Glik, S. Kinayyigit, K. L. Ronayne, M. Towrie, I. V. Sazanovich, J. A. Weinstein and F. N. Castellano, *Inorg. Chem.*, 2008, **47**, 6974–6983.
14 J. Best, I. V. Sazanovich, H. Adams, R. D. Bennett, E. S. Davies, A. J. H. M. Meijer, M. Towrie, S. A. Tikhomirov, O. V. Bouganov, M. D. Ward and J. A. Weinstein, *Inorg. Chem.*, 2010, **49**, 10041–10056.
15 C. J. Adams, N. Fey, Z. A. Harrison, I. V. Sazanovich, M. Towrie and J. A. Weinstein, *Inorg. Chem.*, 2008, **47**, 8242–8257.
16 S. Archer and J. A. Weinstein, *Coord. Chem. Rev.*, 2012, **256**, 2530–2561.
17 S. Chakraborty, T. J. Wadas, H. Hester, R. Schmehl, R. Eisenberg and J. Thaddeus, *Inorg. Chem.*, 2005, **44**, 6865–6878.
18 C.-W. Chan, L.-K. Cheng and C.-M. Che, *Coord. Chem. Rev.*, 1994, **132**, 87–97.
19 M. Hissler, W. B. Connick, D. K. Geiger, J. E. McGarrah, D. Lipa, R. J. Lachicotte and R. Eisenberg, *Inorg. Chem.*, 2000, **39**, 447–457.
20 V. W. Yam, R. P. Tang, K. M. Wong and K.-K. Cheung, *Organometallics*, 2001, **20**, 4476–4482.
21 M. L. Muro, A. A. Rachford, X. Wang and F. N. Castellano, *Top. Organomet. Chem.*, 2010, **29**, 159–191.
22 J. A. Weinstein, M. Delor, I. V. Sazanovich, M. Towrie and P. A. Scattergood, in *XXIV IUPAC symposium on photochemistry*, 2012, p. 120 [PO415].
23 G. Zhou, W.-Y. Wong, S.-Y. Poon, C. Ye and Z. Lin, *Adv. Funct. Mater.*, 2009, **19**, 531–544.
24 P. Nguyen, G. Lesley, T. B. Marder, I. Ledoux and J. Zyss, *Chem. Mater.*, 1997, **9**, 406–408.
25 T. M. Cooper, D. M. Krein, A. R. Burke, D. G. McLean, J. E. Rogers and J. E. Slagle, *J. Phys. Chem. A*, 2006, **110**, 13370–13378.
26 L. Kondrachova, K. E. Paris, P. C. Sanchez, A. M. Vega, R. Pyati and C. D. Rithner, *J. Electroanal. Chem.*, 2005, **576**, 287–294.
27 E. Glimsdal, M. Carlsson, T. Kindahl, M. Lindgren, C. Lopes and B. Eliasson, *J. Phys. Chem. A*, 2010, **114**, 3431–3442.
28 T. M. Cooper, B. C. Hall, A. R. Burke, J. E. Rogers, D. G. Mclean, J. E. Slagle and P. A. Fleitz, *Chem. Mater.*, 2004, **16**, 3215–3217.
29 A. Mohammed, B. Minaev, H. Ågren, M. Lindgren and P. Norman, *Chem. Phys. Lett.*, 2009, **481**, 209–213.
30 S. C. Jones, V. Coropceanu, S. Barlow, T. Kinnibrugh, T. Timofeeva, J.-L. Brédas and S. R. Marder, *J. Am. Chem. Soc.*, 2004, **126**, 11782–11783.
31 L. Liu, D. Huang, S. M. Draper, X. Yi, W. Wu and J. Zhao, *Dalton Trans.*, 2013, **42**, 10694–10706.
32 E. Glimsdal, I. Dragland, M. Carlsson, B. Eliasson, T. B. Melø and M. Lindgren, *J. Phys. Chem. A*, 2009, **113**, 3311–3320.
33 M. S. Khan, M. R. A. Al-Mandhary, M. K. Al-Suti, A. K. Hisahm, P. R. Raithby, B. Ahrens, M. F. Mahon, L. Male, E. A. Marseglia, E. Tedesco, R. H. Friend, A. Köhler, N. Feeder and S. J. Teat, *J. Chem. Soc., Dalton Trans.*, 2002, 1358–1368.
34 C.-H. Tao, N. Zhu and V. W.-W. Yam, *Chem. – Eur. J*, 2005, **11**, 1647–1657.
35 G. Ramakrishna, T. I. Goodson, J. E. Rogers-haley, T. M. Cooper, D. G. Mclean and A. Urbas, *J. Phys. Chem. C*, 2009, **113**, 1060–1066.
36 M.-H. Nguyen and J. H. K. Yip, *Organometallics*, 2012, **31**, 7522–7531.
37 J. M. Keller, K. D. Glusac, E. O. Danilov, S. McIlroy, P. Sreearuothai, A. R. Cook, H. Jiang, J. R. Miller and K. S. Schanze, *J. Am. Chem. Soc.*, 2011, **133**, 11289–11298.
38 R. T. Farley, Q. Zheng, J. A. Gladysz and K. S. Schanze, *Inorg. Chem.*, 2008, **47**, 2955–2963.
39 F. Guo, K. Ogawa, Y.-G. Kim, E. O. Danilov, F. N. Castellano, J. R. Reynolds and K. S. Schanze, *Phys. Chem. Chem. Phys.*, 2007, **9**, 2724–2734.
40 R. Berenguer, J. Ferna, E. Lalinde and S. Sa, *Organometallics*, 2013, **32**, 835–845.
41 C.-J. Lin, C.-Y. Chen, S. K. Kundu and J.-S. Yang, *Inorg. Chem.*, 2014, **53**, 737–745.
42 P. Lind, D. Boström, M. Carlsson, A. Eriksson, E. Glimsdal, M. Lindgren and B. Eliasson, *J. Phys. Chem. A*, 2007, **111**, 1598–1609.
43 W. M. Kwok, D. L. Phillips, P. K. Yeung and V. W. Yam, *J. Phys. Chem. A*, 1997, **101**, 9286–9295.
44 C. L. Choi, Y. F. Cheng, C. Yip, D. L. Phillips and V. W. Yam, *Organometallics*, 2000, **19**, 3192–3196.
45 C. Liao, J. E. Yarnell, K. D. Glusac and K. S. Schanze, *J. Phys. Chem. B*, 2010, **114**, 14763–14771.
46 R. Packheiser, P. Ecorchard, T. Ru and H. Lang, *Organometallics*, 2008, **27**, 3534–3546.
47 W. Wu, J. Zhao, J. Sun, L. Huang and X. Yi, *J. Mater. Chem. C*, 2013, **1**, 705–716.
48 I. V. Sazanovich, M. A. H. Alamiry, A. J. H. M. Meijer, M. Towrie, E. S. Davies, R. D. Bennett and J. A. Weinstein, *Pure Appl. Chem.*, 2013, **85**, 1331–1348.
49 H. Guo, M. L. Muro-Small, S. Ji, J. Zhao and F. N. Castellano, *Inorg. Chem.*, 2010, **49**, 6802–6804.
50 F. N. Castellano, *Dalton Trans.*, 2012, **41**, 8493–8501.
51 D. Gosztola, M. P. Niemczyk, W. Svec, A. S. Lukas and M. R. Wasielewski, *J. Phys. Chem. A*, 2000, **104**, 6545–6551.
52 I. V. Sazanovich, M. A. H. Alamiry, J. Best, R. D. Bennett, O. V. Bouganov, E. S. Davies, V. P. Grivin, A. J. H. M. Meijer, V. F. Plyusnin, K. L. Ronayne, A. H. Shelton, S. A. Tikhomirov, M. Towrie and J. A. Weinstein, *Inorg. Chem.*, 2008, **47**, 10432–10445.

53 J. E. Rogers and L. A. Kelly, *J. Am. Chem. Soc.*, 1999, **121**, 3854–3861.
54 J. E. McGarrah and R. Eisenberg, *Inorg. Chem.*, 2003, **42**, 4355–4365.
55 P. Chen, T. D. Westmoreland, E. Danielson, K. S. Schanze, D. Anthon, P. E. Neveux and T. J. Meyer, *Inorg. Chem.*, 1987, **26**, 1116–1126.
56 T. Takada, K. Kawai, M. Fujitsuka and T. Majima, *J. Am. Chem. Soc.*, 2006, **128**, 11012–11013.
57 G. B. Kauffman, L. A. Teter and J. E. Huheey, *Inorg. Synth.*, 1963, **7**, 245.
58 R. D'Amato, A. Furlani, M. Colapietro, G. Portalone and M. Casalboni, *J. Organomet. Chem.*, 2001, **627**, 13–22.
59 S. Lee, K. R. J. Thomas, S. Thayumanavan and C. J. Bardeen, *J. Phys. Chem. A*, 2005, **109**, 9767–9774.
60 J. E. McGarrah, Y.-J. Kim, M. Hissler and R. Eisenberg, *Inorg. Chem.*, 2001, **40**, 4510–4511.
61 K. Sonogashira, T. Yatake, Y. Tohda, S. Takahashi and N. Hagihara, *J. Chem. Soc., Chem. Commun.*, 1977, 291–292.
62 K. Sonogashira, Y. Fujikura, T. Yatake, N. Toyoshima, S. Takahashi and N. Hagihara, *J. Organomet. Chem.*, 1978, **145**, 101–108.
63 G. G. Mather, A. Pidcock and G. J. N. Rapsey, *J. Chem. Soc., Dalton Trans.*, 1973, 2095–2099.
64 E. Danielson, C. M. Elliott, J. W. Merkert and T. J. Meyer, *J. Am. Chem. Soc.*, 1987, **109**, 2519–2520.
65 P. Jarosz, P. Du, J. Schneider, S.-H. Lee, D. McCamant and R. Eisenberg, *Inorg. Chem.*, 2009, **48**, 9653–9663.
66 M. Hissler, J. E. McGarrah, W. B. Connick, D. K. Geiger, S. D. Cummings and R. Eisenberg, *Coord. Chem. Rev.*, 2000, **208**, 115–137.
67 N. M. Shavaleev, H. Adams, J. Best and J. A. Weinstein, *J. Organomet. Chem.*, 2007, **692**, 921–925.
68 J. M. Keller and K. S. Schanze, *Organometallics*, 2009, **28**, 4210–4216.
69 N. Chawdhury, A. Kohler, R. H. Friend, M. Younus, N. J. Long, P. R. Raithby and J. Lewis, *Macromolecules*, 1998, **31**, 722–727.
70 B. El Hamaoui, F. Laquai, S. Baluschev, J. Wu and K. Müllen, *Synth. Met.*, 2006, **156**, 1182–1186.
71 K. S. Schanze, E. E. Silverman and X. Zhao, *J. Phys. Chem. B*, 2005, **109**, 18451–18459.
72 W. Wu, H. Guo, W. Wu, S. Ji and J. Zhao, *Inorg. Chem.*, 2011, **50**, 11446–11460.
73 K. Nakamaru, *Bull. Chem. Soc. Jpn.*, 1982, **55**, 2697–2705.
74 A. A. Rachford, S. Goeb, R. Ziessel and F. N. Castellano, *Inorg. Chem.*, 2008, **47**, 4348–4355.
75 T. Elsaesser and W. Kaiser, *Annu. Rev. Phys. Chem.*, 1991, **42**, 83–107.
76 K. G. Spears, X. Wen and R. Zhang, *J. Phys. Chem.*, 1996, **100**, 10206–10209.
77 Y. Huang, C. T. Rettner, D. J. Auerbach and A. M. Wodtke, *Science*, 2000, **290**, 111–114.
78 M. J. Potasek and J. J. Hopfield, *Proc. Natl. Acad. Sci. U. S. A.*, 1977, **74**, 3817–3820.
79 A. Troisi, M. A. Ratner and A. Nitzan, *J. Chem. Phys.*, 2003, **118**, 6072–6082.
80 A. Nitzan, *Annu. Rev. Phys. Chem.*, 2001, **52**, 681–750.
81 M. Chergui, *Dalton Trans.*, 2012, **41**, 13022–13029.
82 S. Lentijo, J. A. Miguel and P. Espinet, *Inorg. Chem.*, 2010, **49**, 9169–9177.
83 T. Cardolaccia, A. M. Funston, M. E. Kose, J. M. Keller, J. R. Miller and K. S. Schanze, *J. Phys. Chem. B*, 2007, **111**, 10871–10880.
84 K. Kim, S. Liu, M. E. Kose and K. S. Schanze, *Inorg. Chem.*, 2006, **45**, 2509–2519.
85 E. O. Danilov, I. E. Pomestchenko, S. Kinayyigit, P. L. Gentili, M. Hissler, R. Ziessel and F. N. Castellano, *J. Phys. Chem. A*, 2005, **109**, 2465–2471.
86 D. N. Kozhevnikov, V. N. Kozhevnikov, M. Z. Shafikov, A. M. Prokhorov, D. W. Bruce and J. A. G. Williams, *Inorg. Chem.*, 2011, **50**, 3804–3815.
87 R. M. van der Veen, A. Cannizzo, F. van Mourik, A. Vlček and M. Chergui, *J. Am. Chem. Soc.*, 2011, **133**, 305–315.
88 C. Bressler, C. Milne, V.-T. Pham, A. ElNahhas, R. M. van der Veen, W. Gawelda, S. Johnson, P. Beaud, D. Grolimund, M. Kaiser, C. N. Borca, G. Ingold, R. Abela and M. Chergui, *Science*, 2009, **323**, 489–492.
89 A. Cannizzo, A. M. Blanco-Rodríguez, A. El Nahhas, J. Sebera, S. Zális, A. Vlcek and M. Chergui, *J. Am. Chem. Soc.*, 2008, **130**, 8967–8974.
90 J. N. Schrauben, K. L. Dillman, W. F. Beck and J. K. McCusker, *Chem. Sci.*, 2010, **1**, 405–410.
91 A. C. Bhasikuttan, M. Suzuki, S. Nakashima and T. Okada, *J. Am. Chem. Soc.*, 2002, **124**, 8398–8405.
92 A. El Nahhas, A. Cannizzo, F. van Mourik, A. M. Blanco-Rodríguez, S. Zális, A. Vlcek and M. Chergui, *J. Phys. Chem. A*, 2010, **114**, 6361–6369.
93 R. Heydová, E. Gindensperger, R. Romano, J. Sýkora, A. Vlček, S. Záliš and C. Daniel, *J. Phys. Chem. A*, 2012, **116**, 11319–11329.
94 G. Greetham, P. Burgos, Q. Cao, I. Clark, P. Codd, R. Farrow, M. George, M. Kogimtzis, P. Matousek, A. Parker, M. Pollard, D. Robinson, Z.-J. Xin and M. Towrie, *Appl. Spectrosc.*, 2010, **64**, 1311–1319.
95 A. Blokhin, M. Gelin, O. Buganov, V. Dubovskii, S. Tikhomirov and G. B. Tolstorozhev, *J. Appl. Spectrosc.*, 2003, **70**, 66–72.
96 A. J. Taylor, E. S. Davies, J. A. Weinstein, I. V. Sazanovich, O. V. Bouganov, S. A. Tikhomirov, M. Towrie, J. McMaster and C. D. Garner, *Inorg. Chem.*, 2012, **51**, 13181–13194.
97 J. J. Snellenburg, S. P. Laptenok, R. Seger, K. M. Mullen and I. H. M. van Stokkum, *J. Stat. Software*, 2012, **49**, 1–22.
98 K. M. Solntsev, S. P. Laptenok and P. Naumov, *J. Am. Chem. Soc.*, 2012, **134**, 16452–16455.
99 M. Kullmann, A. Hipke, P. Nuernberger, T. Bruhn, D. C. G. Götz, M. Sekita, D. M. Guldi, G. Bringmann and T. Brixner, *Phys. Chem. Chem. Phys.*, 2012, **14**, 8038–8050.
100 M. J. Frisch, G. W. Trucks, H. B. Schlegel, G. E. Scuseria, J. M. A. Robb, R. Cheeseman, G. Scalmani, V. Barone, B. Mennucci, G. A. Petersson, H. Nakatsuji, M. Caricato,

X. Li, H. P. Hratchian, A. F. Izmaylov, J. Bloino, G. Zheng, J. L. Sonnenberg, M. Hada, M. Ehara, K. Toyota, R. Fukuda, J. Hasegawa, M. Ishida, T. Nakajima, Y. Honda, O. Kitao, H. Nakai, T. Vreven, A. J. J. Montgomery, J. E. Peralta, F. Ogliaro, M. Bearpark, J. J. Heyd, E. Brothers, K. N. Kudin, V. N. Staroverov, R. Kobayashi, J. Normand, K. Raghavachari, A. Rendell, J. C. Burant, S. S. Iyengar, J. Tomasi, M. Cossi, N. Rega, J. M. Millam, M. Klene, J. E. Knox, J. B. Cross, V. Bakken, C. Adamo, J. Jaramillo, R. Gomperts, R. E. Stratmann, O. Yazyev, A. J. Austin, R. Cammi, C. Pomelli, J. W. Ochterski, R. L. Martin, K. Morokuma, V. G. Zakrzewski, G. A. Voth, P. Salvador, J. J. Dannenberg, S. Dapprich, A. D. Daniels, Ö. Farkas, J. B. Foresman, J. V. Ortiz, J. Cioslowski and D. J. Fox, 2009.

101 R. C. Whaley and A. Petitet, *Software: Pract. Exper.*, 2005, **35**, 101–121.

102 A. D. Becke, *J. Chem. Phys.*, 1993, **98**, 5648–5652.

103 A. D. McLean and G. S. Chandler, *J. Chem. Phys.*, 1980, **72**, 5639–5648.

104 X. Cao and M. Dolg, *J. Chem. Phys.*, 2001, **115**, 7348–7355.

105 S. P. Foxon, C. Green, M. G. Walker, A. Wragg, H. Adams, J. A. Weinstein, S. C. Parker, A. J. H. M. Meijer and J. A. Thomas, *Inorg. Chem.*, 2012, **51**, 463–471.

106 B. Mennucci and J. Tomasi, *J. Chem. Phys.*, 1997, **106**, 5151–5158.